



## EEG spatirospectral patterns and their link to fMRI BOLD signal via variable hemodynamic response functions

René Labounek<sup>a,b,c,\*</sup>, David A. Bridwell<sup>d</sup>, Radek Mareček<sup>e</sup>, Martin Lamoš<sup>a,e</sup>, Michal Mikl<sup>e</sup>, Petr Bednářík<sup>f</sup>, Jaromír Baštinec<sup>g</sup>, Tomáš Slavíček<sup>a,e</sup>, Petr Hluštík<sup>c,h</sup>, Milan Brázdil<sup>e</sup>, Jiří Jan<sup>a</sup>

<sup>a</sup> Department of Biomedical Engineering, Brno University of Technology, Technická 12, Brno, 61600, Czech Republic

<sup>b</sup> Department of Biomedical Engineering, University Hospital Olomouc, I. P. Pavlova 6, Olomouc, 77900, Czech Republic

<sup>c</sup> Department of Neurology, Palacký University, I. P. Pavlova 6, Olomouc, 77900, Czech Republic

<sup>d</sup> Mind Research Network, 1101 Yale Blvd. NE, Albuquerque, NM, 87106, USA

<sup>e</sup> Central European Institute of Technology, Masaryk University, Kamenice 735/5, Brno, 62500, Czech Republic

<sup>f</sup> High-Field MR Centre, Department of Biomedical Imaging and Image-Guided Therapy, Medical University of Vienna, Lazarettgasse 14, Vienna, 1090, Austria

<sup>g</sup> Department of Mathematics, Brno University of Technology, Technická 10, Brno, 61600, Czech Republic

<sup>h</sup> Department of Neurology, University Hospital Olomouc, I. P. Pavlova 6, Olomouc, 77900, Czech Republic

### ARTICLE INFO

#### Keywords:

Simultaneous EEG-fMRI  
Group-ICA  
Spatiospectral patterns  
Large scale brain networks  
Multi-subject blind source separation  
Resting-state  
Semantic decision  
Visual oddball

### ABSTRACT

**Background:** Spatial and temporal resolution of brain network activity can be improved by combining different modalities. Functional Magnetic Resonance Imaging (fMRI) provides full brain coverage with limited temporal resolution, while electroencephalography (EEG), estimates cortical activity with high temporal resolution. Combining them may provide improved network characterization.

**New Method:** We examined relationships between EEG spatirospectral pattern timecourses and concurrent fMRI BOLD signals using canonical hemodynamic response function (HRF) with its 1<sup>st</sup> and 2<sup>nd</sup> temporal derivatives in voxel-wise general linear models (GLM). HRF shapes were derived from EEG-fMRI time courses during “resting-state”, visual oddball and semantic decision paradigms.

**Results:** The resulting GLM F-maps self-organized into several different large-scale brain networks (LSBNs) often with different timing between EEG and fMRI revealed through differences in GLM-derived HRF shapes (e.g., with a lower time to peak than the canonical HRF). We demonstrate that some EEG spatirospectral patterns (related to concurrent fMRI) are weakly task-modulated.

**Comparison with existing method(s):** Previously, we demonstrated 14 independent EEG spatirospectral patterns within this EEG dataset, stable across the resting-state, visual oddball and semantic decision paradigms. Here, we demonstrate that their time courses are significantly correlated with fMRI dynamics organized into LSBN structures. EEG-fMRI derived HRF peak appears earlier than the canonical HRF peak, which suggests limitations when assuming a canonical HRF shape in EEG-fMRI.

**Conclusions:** This is the first study examining EEG-fMRI relationships among independent EEG spatirospectral patterns over different paradigms. The findings highlight the importance of considering different HRF shapes when spatiotemporally characterizing brain networks using EEG and fMRI.

### 1. Introduction

Electroencephalography (EEG) and functional Magnetic Resonance Imaging (fMRI) responses capture different aspects of brain network activity. EEG is primarily sensitive synchronous cortical activity, while fMRI measures changes in blood oxygenation throughout the entire brain following neural activity. EEG provides a direct measure of neural activity with high temporal resolution (but poor spatial resolution),

while fMRI provides an indirect measure of neural activity with high spatial resolution (but poor temporal resolution). Since each modality provides a unique picture of neural activity, integrating (i.e. fusing) information across the two modalities provides an improved spatio-temporal characterization of brain networks.

Many different approaches to EEG-fMRI fusion have been developed and implemented (Bénar et al., 2007; Goldman et al., 2002; Laufs et al., 2003a; Mulert et al., 2004). Generally, these techniques examine the

\* Corresponding author at: Department of Biomedical Engineering, Brno University of Technology, Technická 12, Brno, 61600, Czech Republic.

E-mail address: [rlaboune@umn.edu](mailto:rlaboune@umn.edu) (R. Labounek).

relationship (1) between the BOLD signal's time series  $\mathbf{b}$  and a latent signal  $\mathbf{e}$  derived from raw EEG, re-sampled to the fMRI acquisition time, and convolved with the impulse response function (IRF)  $\mathbf{h}$  to account for the hemodynamic delay that follows neural activity (measured directly with EEG).

$$\mathbf{b} \propto \mathbf{e} * \mathbf{h} \quad (1)$$

The existing EEG signal transformations into  $\mathbf{e}$  can be divided into 2 somewhat distinct approaches. The 1<sup>st</sup> approach, often implemented on task data, emphasizes the detection of previously defined EEG waveform shapes (i.e. graphoelements), including evoked or event-related potentials (Bénar et al., 2007; Moosmann et al., 2008; Mulert et al., 2004) or epileptic spikes (Lemieux et al., 2001; Vulliemoz et al., 2010). The 2<sup>nd</sup> most common approach is to integrate EEG spectra with fMRI (Bridwell et al., 2013; de Munck et al., 2009; Goldman et al., 2002; Kilner et al., 2005; Labounek et al., 2015; Laufs et al., 2003b; Mantini et al., 2007; Mareček et al., 2016; Portnova et al., 2018).

The fixed canonical hemodynamic response function (HRF) is the most common IRF used for modeling the relationship between neural activity and the measured fMRI-BOLD signal (Bénar et al., 2007; Goldman et al., 2002; Labounek et al., 2015; Laufs et al., 2003b; Mantini et al., 2007; Mareček et al., 2017; Rosa et al., 2010; Sammer et al., 2007). However, linear combinations of hemodynamic response basis functions (Friston et al., 1998) better account for differences in HRF shape and timings across subjects and brain areas (Jacobs et al., 2009; Mareček et al., 2016; Salek-Haddadi et al., 2006), allowing a more flexible relationship between neural activity (measured with EEG) and fMRI. Alternatively, HRFs may be estimated in a data-driven manner by deconvolution of the EEG and fMRI time courses (Bridwell et al., 2013; de Munck et al., 2007; Wu et al., 2010). Accounting for different HRF properties may be useful since the HRF shape appears to differ depending on tasks, subjects, fMRI voxel location (de Munck et al., 2009 2007), the frequency band of the EEG signal that it is related to (Bridwell et al., 2013; de Munck et al., 2009 2007; Mareček et al., 2016), or due to hemodynamic changes *within* a location, including those that result from focal epilepsy (Jacobs et al., 2009; Salek-Haddadi et al., 2006).

Although estimation of averaged spectral power fluctuations is a promising first approach for processing stochastic stationary and ergodic signals (Goldman et al., 2002; Laufs et al., 2003a; Rosa et al., 2010; Scelocco et al., 2014), it has some limitations. Specifically, the average power spectrum reflects a mixture of processes which differ both spatially and spectrally, and disentangling these distinct processes with blind source separation (BSS) can improve the ability to isolate EEG-fMRI networks. In addition, identifying spectral features at the aggregate group level ensures that individual subject maps and time courses are “filtered” based on high-level features consistent across multiple participants, improving generalizability. Many data driven single-subject (Anemüller et al., 2003; Hyvärinen et al., 2010; Nikulin et al., 2011; Onton et al., 2005; Ramkumar et al., 2012; Shou et al., 2012) or multi-subject (Bridwell et al., 2013; Cong et al., 2013; Congedo et al., 2010; Eichele et al., 2011; Huster et al., 2015; Huster and Calhoun, 2018; Huster and Raud, 2018; Kovacevic and McIntosh, 2007; Lio and Boulinguez, 2013; Ramkumar et al., 2014) blind source separation techniques of EEG spectra have been implemented, decomposing distinct patterns.

Within the present study, we identify associations between data-driven Group-ICA decomposed EEG spatiotemporal maps with concurrent fMRI using GLM's with flexible HRF shapes, drawing from the unique advantages of previous approaches to EEG-fMRI integration. Spatiotemporal decomposition using Group-ICA decomposes spatiotemporal observations at each epoch into a linear summation of independent spatiotemporal component maps (Bridwell et al., 2018), which appear stable over the three investigated paradigms (Labounek et al., 2018, 2019). Within the present study, we examine associations between the stable EEG spatiotemporal pattern time courses and

concurrent fMRI time courses from a visual oddball task – VOT, a semantic decision task – SDT and during “resting state” – RST. Flexible assumptions about HRF shapes between EEG-fMRI time courses are incorporated by including the canonical HRF with its 1<sup>st</sup> and 2<sup>nd</sup> temporal derivatives in a voxel-wise general linear model (GLM) analyses with spatiotemporal map time courses as the regressor. Using this flexible estimate of HRF shape, we show that HRF peak latencies appear earlier than the canonical HRF, and evaluate the resulting differences in EEG-fMRI associations between the visual oddball task, the semantic decision task, and the “resting-state”.

## 2. Methods

### 2.1. Simultaneous EEG-fMRI acquisitions

The scalp EEG data, with reference between Cz and Fz electrodes, were acquired with a MR compatible 32-channel 10/20 EEG system (*BrainProducts, Germany*) with a sampling frequency of 5 kHz. Two channels were used for ECG and EOG. EEG data were acquired simultaneously with fMRI data during gradient echo imaging sequences (1.5 T Siemens Symphony scanner equipped with Numaris 4 System (*Mrease*)). The equipment was identical during acquisitions of the three paradigms described below, and the subjects within two paradigms partially overlapped (i.e. 29 participated in both the resting state and semantic decision paradigms). This study was carried out in accordance with the recommendations of the guidelines of the Masaryk University Ethics committee with written informed consent from all subjects in accordance with the Declaration of Helsinki. The protocol was approved by the Masaryk University Ethics committee. Additional details about the subjects, equipment, and acquisition parameters are provided in (Labounek et al., 2018) and briefly reproduced below for convenience.

#### 2.1.1. Resting state paradigm and fMRI acquisition

Fifty healthy subjects participated in a 15 min “resting-state” experiment (30 right handed men, 20 right-handed women; age 25 ± 5 years). Subjects were instructed to lie still within the fMRI scanner with their eyes closed, not to think of anything specific, and not to fall asleep.

*Gradient echo, echo-planar functional imaging sequence:* TR = 3000 ms; TE = 40 ms; FOV = 220 × 220 mm; FA = 90°; matrix size 64 × 64 (3.9 × 3.9 mm); slice thickness = 3.5 mm; and 32 transverse slices covering the whole brain except part of the cerebellum. 300 functional scans were acquired in 1 continuous session.

#### 2.1.2. Visual oddball paradigm and fMRI acquisition

An event-related visual oddball task was performed by 21 healthy subjects (13 right-handed men, 1 left-handed man, 7 right-handed women; age 23 ± 2 years). Three stimulus types were presented randomly to each subject. Each stimulus consisted of a single yellow uppercase letter shown for 500 ms on a black background. Inter-stimulus intervals were either 4, 5 or 6 s (drawn uniformly and randomly). A total of 336 stimuli were presented, consisting of targets (letter X, 15%), frequent (letter O, 70%) and distractors (letters other than X and O, 15%). Subjects were instructed to press a button held in their right hand whenever the target stimulus appeared and not to respond to distractor or frequent stimuli. The experiment was divided into 4 sessions for each person (84 stimuli per single-session) (Brázdil et al., 2007).

*Gradient echo, echo-planar functional imaging sequence:* TR = 1660 ms; TE = 45 ms; FOV = 250 × 250 mm; FA = 80°; matrix size = 64 × 64 (3.9 × 3.9 mm); slice thickness = 6 mm; 15 transverse slices covering the whole brain except part of the cerebellum. The task was divided into four equal runs of 256 scans and 84 stimuli.

#### 2.1.3. Semantic decision paradigm and fMRI acquisition

A semantic decision task was performed by 42 healthy subjects (22

right-handed men, 2 left-handed men, 18 right-handed women; age  $25 \pm 5$  years). The task was designed with a block stimulation paradigm, which elicits robust language network activation (Gartus et al., 2009). During the probe block, sentences with semantic error created by a phonemic exchange (e.g. The cat was chased by fog) were presented randomly among semantically correct sentences. The sentences were replaced with a series of the X's or O's, (e.g. 'XXXX xx xxxx xxx.') during the control block. Nine control and eight probe blocks alternated during the experiment. Each block lasted 24 s, and consisted of six different control or probe stimuli presented for 3.5 s followed by a black screen for 0.5 s. Subjects viewed the stimuli through a mirror mounted on the head coil. Responses were not requested from the subjects during the task. After the session, no subjects reported any problems with reading the sentences (Mareček et al., 2016).

*Gradient echo, echo-planar functional imaging sequence:* TR = 1850 ms, TE = 40 ms, FOV =  $250 \times 250$  mm; FA =  $80^\circ$ , matrix size =  $64 \times 64$  ( $3.9 \times 3.9$  mm); slice thickness = 6 mm; no gap between slices; 20 transverse slices covering the whole brain except part of the cerebellum. 228 functional scans were acquired in 1 continuous session.

#### 2.1.4. High resolution anatomical MRI acquisition

Following simultaneous EEG-fMRI measurements, high-resolution anatomical T1-weighted images were acquired using an MPRAGE sequence with 160 sagittal slices, matrix size  $256 \times 256$  resampled to  $512 \times 512$ ; TR = 1700 ms; TE = 3.96 ms; FOV = 246 mm; FA =  $15^\circ$ ; and slice thickness = 1.17 mm.

#### 2.2. EEG data preprocessing

The EEG data were preprocessed as described in (Labounek et al., 2018) using BrainVision Analyzer 2.02 (BrainProducts, Germany). Gradient artifacts were removed using template subtraction (Allen et al., 2000) and signals were resampled to 250 Hz (antialiasing filter included), and filtered with a Butterworth zero phase 1 Hz–40 Hz band-pass filter. Cardiobalistogram artifacts were removed by subtracting the average pulse artifact waveform from each channel (Allen et al., 1998) and signals were re-referenced to the average. For VOT EEG data, eye-blink artifacts were removed by conducting a temporal ICA decomposition and removing eye-blink artifacts visually identified from the back-reconstructed time course. These artifacts were not removed from the SDT dataset in order to determine whether they appear as a group component within the spatirospectral group-ICA decomposition.

#### 2.3. EEG spatirospectral decomposition

EEG spatirospectral decomposition (Eq. (2)) decomposes the matrix of spatirospectral maps  $E$  of dimensions  $E(n_t, n_c * n_\omega)$  into a source matrix  $S$  of dimensions  $S(m, n_c * n_\omega)$  containing independent spatirospectral patterns and a mixing matrix  $W$  of dimensions  $W(n_t, m)$  containing the patterns' dynamics, as described in (Bridwell et al., 2013; Labounek et al., 2018). Dimension  $n_t$  represents the number of spatirospectral epochs ( $n_t = 540$  for RST;  $n_t = 255$  for SDT;  $n_t = 256$  for VOT; epoch length 1.66 s for each dataset, i.e. the shortest TR time of fMRI acquisitions), dimension  $n_c$  is the total number of leads ( $n_c = 30$ ), dimension  $n_\omega$  is the total number of absolute valued and squared spectral coefficients ( $n_\omega = 67$ ) and dimension  $m$  is the number of decomposed orthogonal and independent spatirospectral components ( $m = 20$ ).

$$E = WS \quad (2)$$

As previously implemented in (Labounek et al., 2018) using the GIFT toolbox (<http://mialab.mrn.org/software/gift/>) (Calhoun et al., 2001), the matrix  $E$  was dimensionally reduced using PCA (single-subject reduction to 50 principle components and group-based reduction to 20 components), followed by INFOMAX ICA (Bell and Sejnowski, 1995) with 10 ICASSO runs (Himberg et al., 2004).

Individual subject time courses were generated by PCA based back-reconstruction (i.e. the individual partition of the PCA reducing matrix is multiplied by the individual partition of the aggregate reducing matrix) (Calhoun et al., 2001) of the group spatirospectral patterns on the individual subject spatirospectral maps and time-courses. As described in further detail in (Labounek et al., 2018), k-means clustering was conducted on the entire set of back-reconstructed components from the 3 group ICA runs. An alternative approach would be to compute group ICA on the entire 3 paradigm dataset, however, our goal was to determine whether these components were present within *independent* runs of group ICA, since this suggests that the observed components are stable will be present in subsequent studies using potentially different acquisition parameters, paradigms, and subject populations. Within the present study we focus on the individual time-courses of these 14 stable group components.

#### 2.4. Topologies and average spectral densities of stable spatirospectral patterns

The topology  $t_m$  of each group-averaged  $m$ -th spatirospectral pattern was estimated with Eq. (3) as the sum of spatirospectral pattern  $S_m$  over frequencies, normalized to a mean of 0 and standard deviation of 1 with Eq. (4), where  $\bar{t}_m$  is the mean value and  $\sigma_{t_m}$  is variance of the unnormalized vector  $t_m$ . The average spectral density  $d_m(\omega)$  of each  $m$ -th group averaged spatirospectral pattern was calculated with Eq. (5) as the averaged sum of  $m$ -th spatirospectral pattern  $S_m$  over channels  $c$ . Its confidence interval was computed over channels with Eqs. (6) and (7), where  $\sigma_{d_m}(\omega)$  is the variance of the spectral density for each frequency  $\omega$ . The similarity of topologies over different datasets was estimated by computing the Pearson correlation coefficient among pairs. These coefficients were transformed to t-values and p-values (using Eqs. (2) and (3) in (Labounek et al., 2018)).

$$t_m(c) = \sum_{n=1}^{n_\omega} S_m(c, n) \quad (3)$$

$$\bar{t}_{mN(0,1)} = \frac{t_m - \bar{t}_m}{\sigma_{t_m}} \quad (4)$$

$$d_m(\omega) = \frac{1}{n_c} \sum_{k=1}^{n_c} S_m(k, \omega) \quad (5)$$

$$\sigma_{d_m}(\omega) = \frac{1}{n_c - 1} \sum_{k=1}^{n_c} (S_m(k, \omega) - d_m(\omega)) \quad (6)$$

$$d_m = \langle \bar{d}_m - 2\sqrt{\sigma_{d_m}}, \bar{d}_m + 2\sqrt{\sigma_{d_m}} \rangle \quad (7)$$

#### 2.5. fMRI data preprocessing

The fMRI data were preprocessed with SPM8 (Wellcome Trust Centre for Neuroimaging, London, UK) software library. Motion artifacts were minimized by alignment of all functional scans, followed by co-registration with the subject's anatomical image and normalization into standardized MNI space (Montreal Neurological Institute template) (Friston et al., 1995). Functional scans were spatially smoothed with an isotropic 3D Gaussian filter (FWHM = 8 mm) to increase the signal to noise ratio (SNR) and to make the random errors more normally distributed. Periods longer than 128 s were linearly detrended to remove slow drifts and physiological noise.

#### 2.6. EEG-fMRI fusion (general linear modeling and variable HRFs)

Individual subject EEG spatirospectral map time courses (i.e. mixing matrices or weights) were derived by back-reconstructing individual subject data on the group derived spatirospectral components. Thus, each spatirospectral map has a weight which corresponds to each fMRI

acquisition. Relationships between fMRI voxel time courses and spatiotemporal map time courses were examined using the general linear model with the individual time course convolved with the canonical HRF (regressor 1), convolved with the 1<sup>st</sup> temporal derivative of the HRF (regressor 2) or convolved with the 2<sup>nd</sup> temporal derivative of the HRF (regressor 3) as in (Mareček et al., 2016). Using the canonical HRF and 1<sup>st</sup> and 2<sup>nd</sup> temporal derivatives helps account for variability in the HRF's shape across subjects, tasks, and voxels.

$$Y = X\beta + \varepsilon \quad (8)$$

Separate general linear models (GLMs, Eq. (8)) (Friston et al., 1994) were performed for each stable spatiotemporal pattern, paradigm and subject. In addition to the three EEG regressors, the model matrix  $X$  contained a DC component. Regression matrices  $\beta$  were estimated over all GLMs with the ReML algorithm (Restricted Maximum Likelihood) implemented in SPM12 software (Wellcome Trust Centre for Neuroimaging, London, UK) in the MATLAB programming environment (MathWorks, Natick, USA).

Group-averaged EEG-fMRI results were estimated with a one-way ANOVA test (implemented in SPM12) of 3 EEG-derived single-subject spatial  $\beta$ -maps for each of 3 EEG regressors. The  $\beta$  weights served as dependent variables in separate ANOVA tests conducted for each paradigm and spatiotemporal pattern (i.e. 3 paradigms \* 14 stable spatiotemporal patterns = 42 tests), generating group-averaged spatial EEG-fMRI  $F$ -maps. The final  $F$ -maps were thresholded at  $p < 0.001$  uncorrected for multiple statistical tests (i.e. with a critical absolute  $F$ -value of 5.71), and the criteria that clusters contain 100 voxels or more.

## 2.7. Estimations of group-averaged HRFs

For each supra-threshold voxel  $i$ , the local EEG-fMRI HRF  $\mathbf{h}_i$  was estimated with Eq. (9), where  $\beta_{i,1}$  is the group-averaged regression coefficient of the 1<sup>st</sup> EEG regressor (convolved with the canonical HRF  $\mathbf{r}$ ),  $\beta_{i,2}$  is the group-averaged regression coefficient of the 2<sup>nd</sup> EEG regressor (convolved with 1<sup>st</sup> temporal ( $t$ ) derivation of canonical HRF), and  $\beta_{i,3}$  is the group-averaged regression coefficient of the 3<sup>rd</sup> EEG regressor (convolved with 2<sup>nd</sup> temporal derivation of canonical HRF) as implemented in (Friston et al., 1998). The distributions of estimated HRFs were examined across supra-threshold voxels, separately for each spatiotemporal pattern, and paradigm. Peak timings were identified from the median resulting curves and were compared to the timing of the canonical HRF absolute peak.

$$\mathbf{h}_i = \beta_{i,1}\mathbf{r} + \beta_{i,2}\frac{d\mathbf{r}}{dt} + \beta_{i,3}\frac{d^2\mathbf{r}}{dt^2} \quad (9)$$

## 2.8. Relationship between EEG spatiotemporal time-courses and stimuli vectors

The relationship between EEG spatiotemporal time-courses and experimental stimuli were compared with a single-subject GLM and a group  $t$ -test as implemented and described in (Labounek et al., 2018). For each subject, paradigm and session, we have one matrix  $\mathbf{W}$  with dimensions  $\mathbf{W}(n_t, 20)$  containing the back-reconstructed time course of each spatiotemporal component. Relationships between these dynamics and stimulus vector timings (in matrix  $\mathbf{X}$ ) were assessed with a single-subject general linear model (Eq. (10), GLM) solved with the least mean square algorithm (Eq. (11)), and a continuous group one-sample  $t$ -test for the  $k$ -th stimulus vector (Eq. (12)) as implemented previously (Friston et al., 1994; Labounek et al., 2015). Variable  $\mathbf{c}$  sets the contrast at the stimulus vector of interest, the brackets  $\langle \rangle$  characterize the expectation over subjects, variable  $\sigma$  is the standard deviation and variable  $s$  is the total number of subjects.

For VOT data, model matrix  $\mathbf{X}$  contained frequent, target and distractor timings in 12 separate binary vectors for each stimulus and session and 4 vectors for the DC component in each session. For SDT

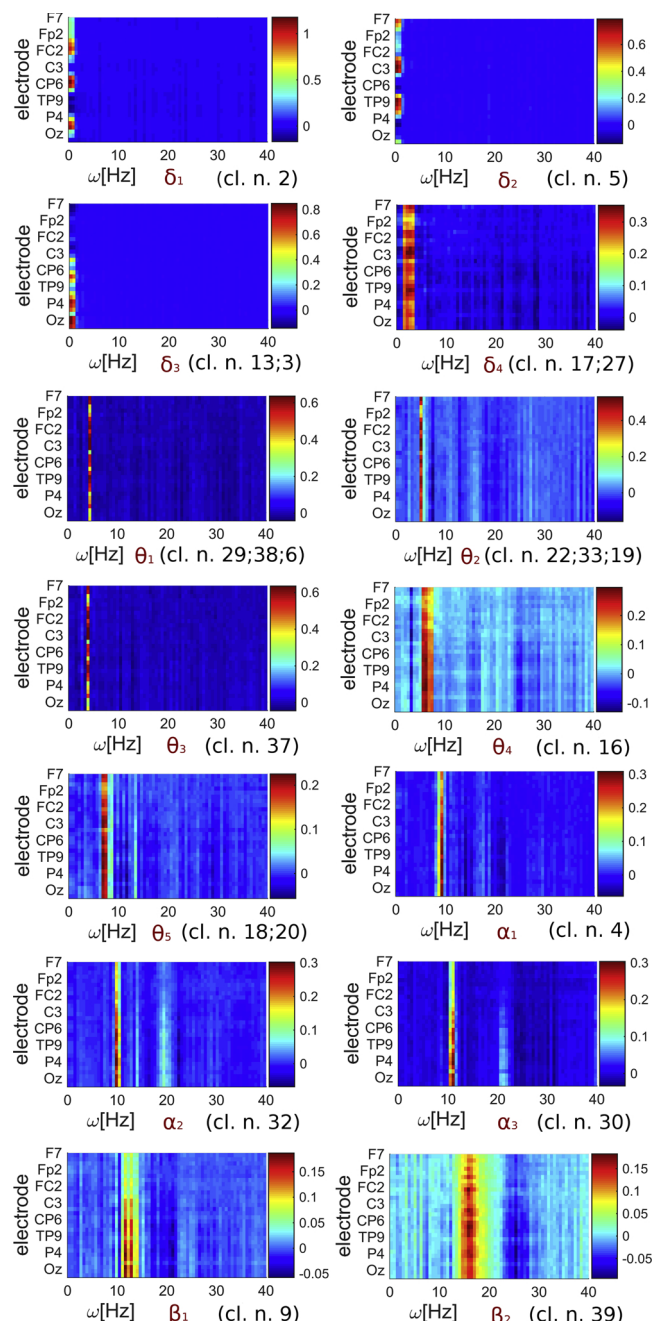


**Fig. 1.** Fourteen stable independent EEG spatiotemporal patterns present within RST, SDT and VOT datasets. Each pattern represents orthogonal and independent spatiotemporal power patterns observed in all three datasets (see Labounek et al., 2018). The red label below each plot indicates which of the conventional EEG frequency bands the pattern fall within, i.e.  $\delta$ =(0–4 Hz);  $\theta$ =(4–8 Hz);  $\alpha$ =(8–12 Hz);  $\beta$ =(12–30 Hz). These labels are used to refer to the patterns throughout the manuscript.

data, model matrix  $\mathbf{X}$  contained a binary vector with the probe block timings and a vector with the DC component.

$$\mathbf{W} = \mathbf{X}\beta + \varepsilon \quad (10)$$

$$\beta = (\mathbf{X}^T \mathbf{X})^{-1} \mathbf{X}^T \mathbf{W} \quad (11)$$

$$t_k = \sqrt{s} \frac{\langle \mathbf{c}_k^T \beta_k \rangle}{\sigma_{\langle \mathbf{c}_k^T \beta_k \rangle}} \quad (12)$$

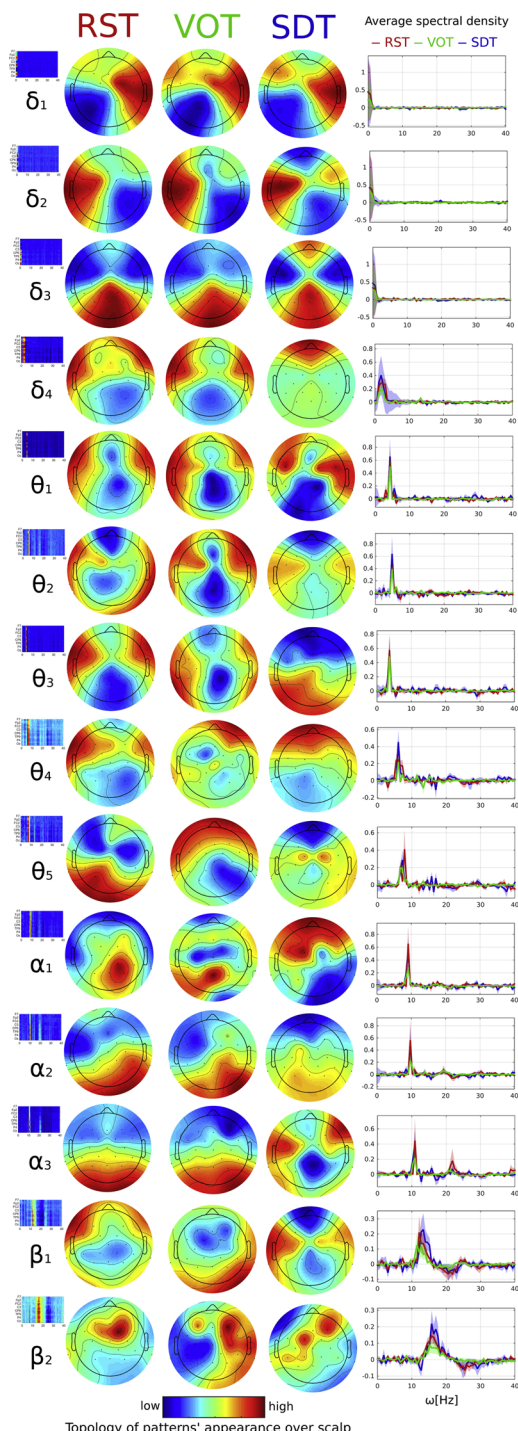


**Fig. 2.** Scalp topologies  $t_m$  of EEG spatiotopographic patterns and their average spectral densities  $d_m$  for RST, SDT and VOT datasets. From the spatiotopographic maps, topologies were calculated with Eqs. (3) and (4) and spectral densities were calculated with Eqs. (5)–(7). The shaded regions within the spectral density plots indicate the 95% confidence interval of the mean for RST (red), VOT (green), and SDT (blue). The units are not included for the topographic maps since each map was normalized to a mean of 0 and a standard deviation of 1.

### 3. Results

#### 3.1. Stable EEG spatiotopographic patterns, their topologies and spectral densities

We focused on fourteen spatiotopographic patterns that were previously demonstrated to be stable over all three paradigms (Fig. 1). The topographies appear smooth across the scalp and spectral densities of the 14 stable spatiotopographic patterns generally fall within frequency bands characteristic of human EEG (Fig. 2). Four of the 14 topographies appear similar between 2 out of the 3 datasets ( $\delta_4$ ,  $\theta_3$ ,  $\alpha_3$  and  $\beta_2$ ), while 6 of the 14 topographies appear similar across all 3 datasets ( $\delta_{1-3}$ ,  $\theta_{1-2}$  and  $\alpha_2$ ); see Table 1 and Fig. 2. The spatiotopographic patterns generally demonstrate similar topographies across the RST and VOT datasets, while the SDT dataset appears corrupted by eye-blink artifacts as described later. A more detailed description of intra-cluter and inter-subject similarities among topographies can be found in Figs. 4 and 5 within (Labounek et al., 2018).

The independent spatiotopographic maps potentially differ due to differences in topography or spectral peak. For example, three independent low  $\delta$ -band (0–1.5 Hz) patterns show peak topographic responses over right temporal regions ( $\delta_1$ ), left temporal regions ( $\delta_2$ ), and occipital/parietal regions ( $\delta_3$ ). The high  $\delta$ -band (1.5 Hz–4 Hz;  $\delta_4$ ) and  $\theta$ -band (4–8 Hz;  $\theta_{1-4}$ ) patterns are spatially similar with bilateral peaks located over frontal and fronto-temporal areas, with a peak decrease around the midline. Cluster  $\theta_5$  demonstrates the highest power within the upper  $\theta$ -band, but differs in scalp topography across datasets. Three independent  $\alpha$ -band (8–12 Hz;  $\alpha_{1-3}$ ) patterns were present with spatially different topographies (i.e. central-parietal areas for  $\alpha_1$ , bilateral occipital areas for  $\alpha_3$  and right occipital areas for  $\alpha_2$ ). The low  $\beta$ -band (10–15 Hz;  $\beta_1$ ) pattern differs spatially across tasks and the high  $\beta$ -band (12–20 Hz;  $\beta_2$ ) pattern shows peak power around right frontal and fronto-central areas.

#### 3.2. EEG-fMRI F-maps

FMRI F-maps were generated with the individual EEG spatiotopographic time-courses as regressors (Fig. 3 and Supplementary Material). While 12 of 14 F-maps demonstrate supra-threshold voxels for the VOT task, 9 of 14 were supra-threshold for RST, and only 4 of 14 were supra-threshold for SDT. In terms of absolute F-values, the strongest values were observed for VOT data. The values are lower for the RST and SDT datasets except for the SDT EEG-fMRI map corresponding to  $\delta_4$ -band. This pattern appears to reflect eye-blinking artifacts, however, as suggested by Fig. 2 and in (Labounek et al., 2018). The robust supra-threshold activations in visual cortices (Fig. 3) support the hypothesis that this result is due to shared physiological noise between the two signals, and not due to relationships between the EEG and fMRI signals directly. The other 3 SDT supra-threshold maps show similarity with RST and VOT maps for the corresponding EEG patterns (Fig. 3 and Supplementary material).

Significant EEG-fMRI activations were observed for the VOT task within sensory-motor and basal ganglia networks for high  $\delta_4$ -band and  $\theta_{1-4}$ -band patterns (similar locations were present with lower F-values and lower cluster size within the RST and SDT datasets) (Figs. 3, 4a and Suppl. Material). EEG-fMRI networks partially overlapped for  $\delta_{1-2}$ -band and low  $\beta_1$ -band patterns (Fig. 6 and Suppl. Material). The  $\delta_{1-2}$ -band F-statistic patterns overlapped with the basal ganglia, while the low  $\beta_1$ -band pattern overlapped with the left lateralized sensory-motor areas (i.e. consistent with the relationship between its time-course and the frequent stimulus vector, demonstrated in Table 2). The 3<sup>rd</sup>  $\delta_3$ -band pattern demonstrates supra-threshold F-values within the basal ganglia for the RST data.

The independent  $\alpha$ -band patterns (with differing topographies; Fig. 2) correspond with fMRI activity within non-overlapping voxels within the VOT task (Fig. 5). The  $\alpha_2$ -band pattern is unrelated to the

**Table 1**

Similarities of EEG spatiotopographic pattern topologies evaluated with Pearson correlation coefficients and their following p-values over the three possible pairs of datasets. Bold highlighted are p-values with threshold value  $p < 0.001$  uncorrected for 3 independent multiple comparisons. Number of samples was 30 (electrodes) and there was 1° of freedom.

Cl.	Pearson correlation coefficients			p-values			Band
	RST-VOT	RST-SDT	VOT-SDT	RST-VOT	RST-SDT	VOT-SDT	
$\delta_1$	0.906	0.963	0.950	<b>0.00000</b>	<b>0.00000</b>	<b>0.00000</b>	δ
$\delta_2$	0.982	0.885	0.871	<b>0.00000</b>	<b>0.00000</b>	<b>0.00000</b>	
$\delta_3$	0.973	0.925	0.855	<b>0.00000</b>	<b>0.00000</b>	<b>0.00000</b>	
$\delta_4$	0.852	0.136	-0.122	<b>0.00000</b>	0.47768	0.51887	
$\theta_1$	0.892	0.694	0.562	<b>0.00000</b>	<b>0.00002</b>	0.00119	θ
$\theta_2$	0.571	0.631	0.534	<b>0.00092</b>	<b>0.00018</b>	0.00231	
$\theta_3$	0.676	-0.529	0.120	<b>0.00004</b>	0.00259	0.52574	
$\theta_4$	0.093	0.563	0.259	0.62587	0.00115	0.16577	
$\theta_5$	-0.362	-0.065	-0.412	0.04902	0.73328	0.02339	
$\alpha_1$	0.168	-0.559	-0.222	0.37449	0.00129	0.23778	α
$\alpha_2$	0.923	0.649	0.616	<b>0.00000</b>	<b>0.00010</b>	<b>0.00028</b>	
$\alpha_3$	0.938	-0.475	-0.461	<b>0.00000</b>	0.00787	0.01012	
$\beta_1$	0.034	0.461	-0.044	0.85853	0.01013	0.81552	β
$\beta_2$	0.132	0.591	-0.196	0.48528	<b>0.00055</b>	0.29783	

stimulus timings (Table 2), despite its association with deactivations in primary visual cortical fMRI responses (Figs. 3, 5a and Suppl. Material). The  $\alpha_1$ -band pattern was associated with deactivations within secondary visual cortical fMRI regions, which are associated with target stimulus timings (Fig. 5b, Table 2 and Suppl. Material). This finding indicates that the  $\alpha_1$ -band pattern which covaries with secondary visual cortical fMRI fluctuations may be related to cognitive processes that are related to processing target stimuli. The  $\alpha_3$ -band pattern corresponds with deactivations in sensory-motor cortices, secondary visual cortices and left superior frontal gyrus, with activations in the default mode network, left paracentral lobule and right insula (Fig. 5c and Suppl. Material). Results in Table 2 indicate that it is related to frequent stimulus timings.

The high  $\beta_2$ -band pattern, with consistent topographies across paradigms (Fig. 2), is associated with supra-threshold F-map activations within the salience network during VOT. However, results in Table 2 indicate that it is unrelated to stimulus timings (Fig. 6 and Suppl. Material). For RST and SDT datasets, we generally observed less significant, but similar, F-statistic overlays for  $\theta_{1,4}$ -band patterns compared to VOT. In addition, within RST we observe F-statistic map activations within the attention network for the low and high  $\beta_{1,2}$ -band patterns, the  $\theta_5$ -band pattern and the  $\alpha_2$ -band pattern (see in Figs. 4b, 6 and Suppl. Material).

### 3.3. EEG-fMRI impulse response functions

Figs. 3, 6 and the Suppl. Material demonstrate the distribution of estimated HRFs across supra-threshold voxels. From those distributions, Fig. 4 demonstrates the median-derived HRFs over different spatiotopographic patterns for several brain networks. Fig. 5 demonstrates local HRFs for 3 independent  $\alpha_{1,3}$ -band patterns from the EEG-fMRI supra-threshold clusters within the VOT dataset. Fig. 7 demonstrates that the latency of the estimated HRF peaks occur 0.5–2 s prior to the latency of the canonical HRF.

The VOT HRFs generated from the  $\alpha_{1,3}$ -band patterns primarily demonstrate negative peaks with similar timings as the canonical HRF (Fig. 5). The positive HRF peaks derived from the  $\alpha_2$ -band pattern also demonstrate similar timings as the canonical HRF (Fig. 5c). While VOT mean-derived HRFs with the EEG  $\delta_{1,2}$ -band components demonstrate positive HRF peaks, the RST mean-derived HRFs with the EEG  $\delta_3$ -band occipital/parietal component demonstrate negative HRF peak. Each show supra-threshold and significant F-statistics within the basal ganglia (Suppl. Material).

It is interesting to note the discrepancy between the canonical HRF and the HRF derived from attention network activity during RST ( $\theta_5, \beta_1$ ,

$\alpha_2$ ) (Figs. 4b, 6 and Suppl. Material). These results suggest that the canonical HRF (i.e. the HRF without its temporal derivatives) is inadequate for capturing the relationship between those EEG patterns and BOLD-RST data within the attention network.

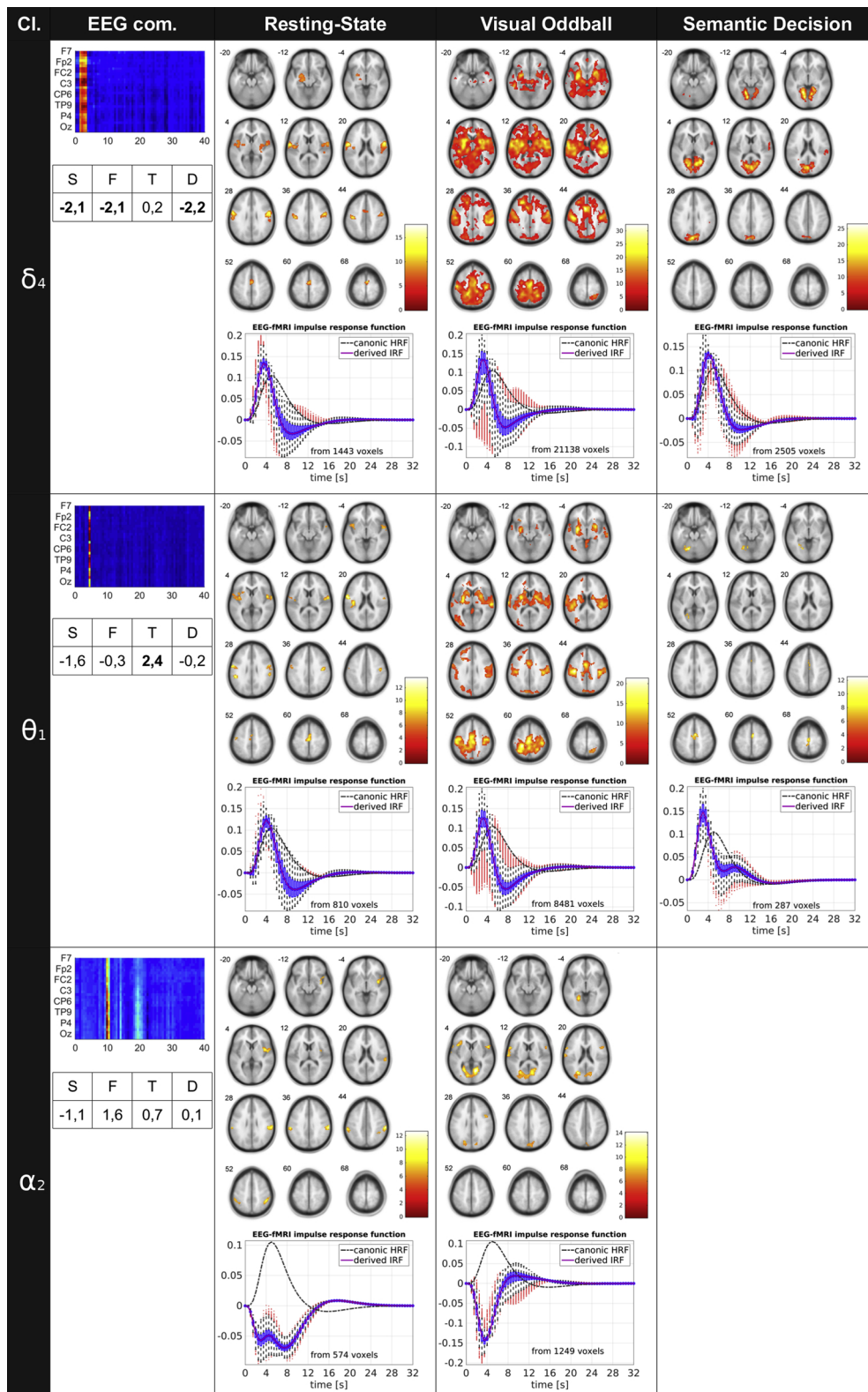
## 4. Discussion

### 4.1. Brain rhythms and scalp EEG topologies

Previously, we demonstrated 14 spatiotopographic EEG components from Group ICA that were consistent across RST, VOT, and SDT paradigms (Labounek et al., 2018). Fluctuations within these components likely contribute to behavior and cognitive function, which may be further revealed by examining the correspondence between these spatiotopographic time courses and concurrent BOLD fMRI responses. Before examining these associations, however, it is important to consider the potential functional roles of these spatiotopographic components given the prior EEG literature demonstrating distinct functions of different EEG frequency bands.

The  $\delta_{1,3}$ -band patterns possibly correspond with or are related to infra-slow EEG patterns (< 1 Hz) (Hiltunen et al., 2014; Keinänen et al., 2018). A recent proposal suggests that slow δ-band oscillations are associated with the ancient systems present in the brains of lower vertebrates (reptilian, amphibian, and fish), and implicates these oscillations in processes involved in monitoring autonomic function (e.g. breathing, heart beat). These oscillations appear to arise and be modulated by deep brain structures, and are associated with slow-wave sleep, and some pathologies (Knyazev, 2012). Consistent with this proposal, we identified two bilateral temporal sources in the present study with responses within these  $\delta_{1,2}$ -bands (Fig. 2) with supra-threshold EEG-fMRI F-statistic maps that show significant values within deeper brain structures (Suppl. material). Positive HRF peaks were observed for temporal spatiotopographic patterns ( $\delta_{1,2}$ ), and negative HRF peaks were observed for the 3rd  $\delta_3$ -band spatiotopographic pattern which demonstrates a negative topographic peak over temporal regions and a positive topographic peak over occipito-parietal topology (Fig. 2).

One high  $\delta_4$ -band and three  $\theta_{1,3}$ -band spatiotopographic patterns demonstrated prominent activity within bilateral frontal or fronto-temporal regions, with activity reduced around the midline (Fig. 2). Previous experiments indicate that frontal θ-band oscillations modulate cognitive control (Cavanagh and Frank, 2014), especially during working memory (Gevins et al., 1979; Jensen and Tesche, 2002; Onton et al., 2005; Sammer et al., 2007). These components potentially contribute to these functions, although they demonstrate bilateral frontal topographic peaks, instead of the mid-central frontal peak typically

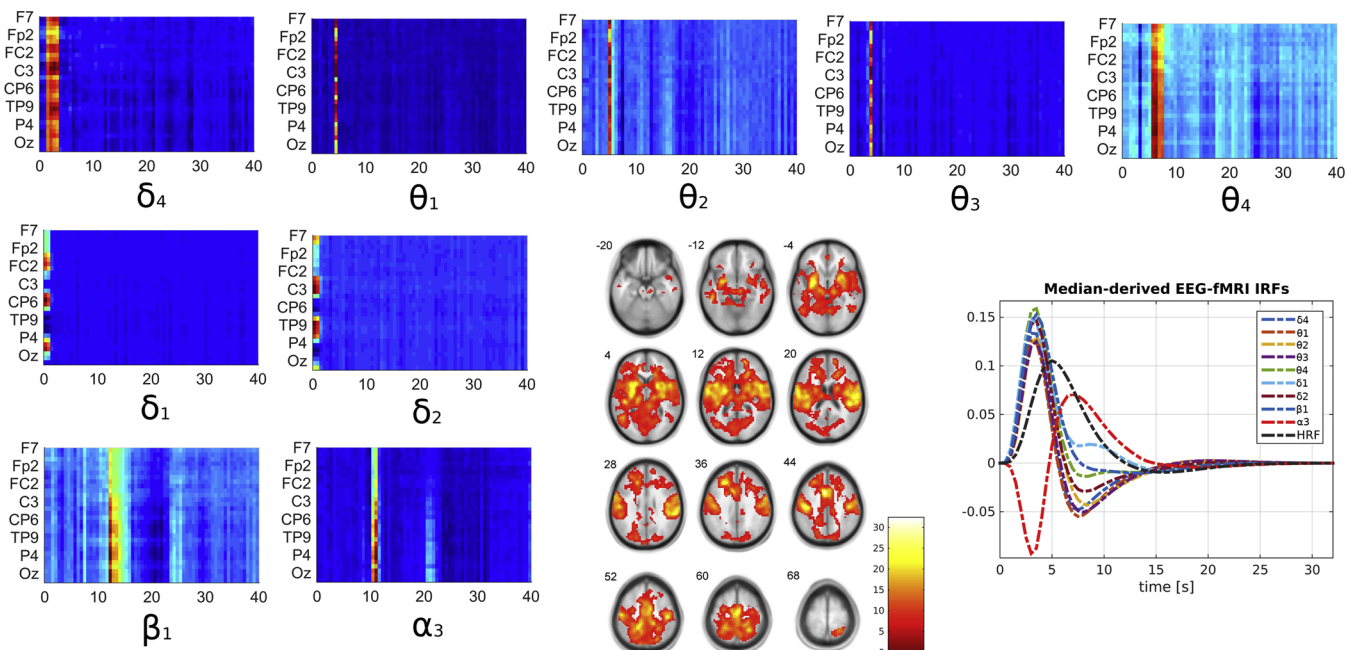


**Fig. 3.** Supra-threshold group-averaged EEG-fMRI results for three different EEG spatiotemporal patterns and RST, VOT and SDT datasets. In the plot below each fMRI map, the black dashed-dotted line represents the canonical HRF, and the purple line represents our median-derived IRF from the white boxplots, where blue oblongs are quartiles and red dots are outliers. The spatiotemporal patterns are indicated on the column on the left, and F-statistic results are overlayed on the fMRI maps if there are 100 contiguous voxels with  $p < 0.001$ . The colorbar indicates the F values in the corresponding map. The values in the table under each pattern are group-averaged t-values of the statistical significance between the spatiotemporal pattern dynamics and the stimulus vectors (S – sentence block in SDT, F – frequent, T – target, D – distractor in VOT). Results are provided for all 14 stable patterns within in the Supplementary Material.

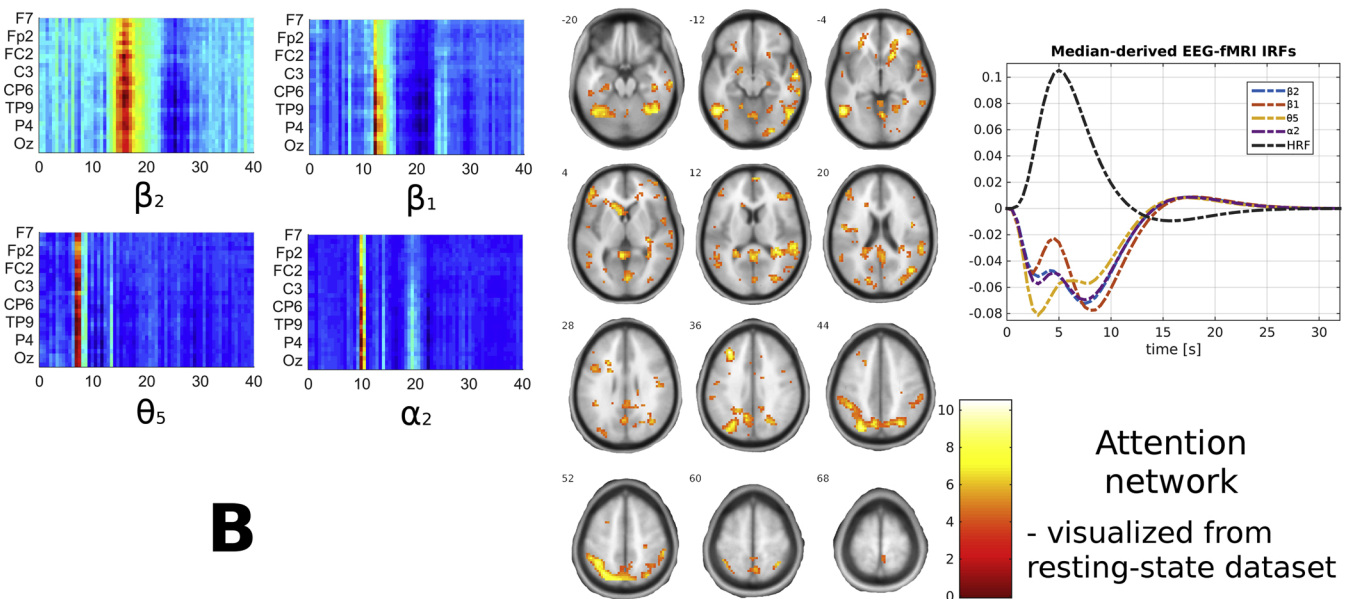
observed.

Three independent spatiotemporal patterns represent occipital and parieto-occipital responses within the  $\alpha_{1-3}$ -band (Fig. 2). For two of the patterns ( $\alpha_{2-3}$ ), we found that decreases correspond to increases in frontal fMRI areas, supporting the associations between  $\alpha$ -band oscillations and active cognitive processes (Klimesch, 1999; Klimesch et al., 2007).

The low  $\beta_1$ -band topologies appear inconsistent across datasets, despite the similarity in their peak frequency (Fig. 2), while the high  $\beta_2$ -band topologies appear to have similar generators (i.e. are consistent across datasets) in right frontal areas (Fig. 2). This finding indicates that  $\beta$ -band responses are present for each paradigm, but the spatial topography of low  $\beta_1$ -band components differs more across paradigms than the high  $\beta_2$ -band components.

**A**

Sensory-motor and basal ganglia networks

**B**

**Attention network**  
- visualized from resting-state dataset

**Fig. 4.** Sensory motor and basal ganglia EEG-fMRI networks observed during VOT and attention EEG-fMRI networks observed during RST. Supra-threshold fMRI voxels were generally present for GLMs constructed from spatiotemporal time courses for VOT (A) and RST (B). Median-derived EEG-fMRI HRF's are indicated on the plot on the right, with positive deviations indicating positive associations between EEG and fMRI and negative deviations indicating that increases in EEG time courses are associated with reductions in fMRI activity. Positive deviations were observed in (A) for all maps except  $\alpha_3$ . The median-derived HRF peaks appear before the canonical HRF peak for all maps in (A). Additional fMRI maps are displayed within the **Suppl. Material**. Within (B), the results derived from the four spatiotemporal maps demonstrate similar HRF shapes, but somewhat different supra-threshold fMRI maps at the level of statistical significance  $p < 0.001$ . The fMRI map is displayed for  $\beta_1$  at a lower statistical threshold ( $p < 0.01$ ) to improve the visibility of the clusters. Additional maps are included within **Suppl. Material**.

#### 4.2. Self-organized EEG-fMRI large scale brain networks

Several functionally distinct LSBNs have been reported during the ‘resting-state’ (Allen et al., 2011; Damoiseaux et al., 2006; Van Den Heuvel et al., 2009) and during tasks (Calhoun et al., 2008; Spadone et al., 2015). Comparison of fMRI LSBNs’ dynamics (derived primarily using spatial group-ICA) with simultaneously acquired EEG shows that some networks (i.e. ventral attention, core and visual networks) correspond to event related potential (ERP) amplitudes (Mantini et al., 2010 2009). In addition, a subset of LSBNs correspond a subset of EEG

power fluctuations (Bridwell et al., 2013; Hlinka et al., 2010; Mantini et al., 2007; Mareček et al., 2017). Although the voxel-wise analysis does not take into account information about LSBN structure, the supra-threshold maps often organize into these structures for a subset of spectral responses (e.g. the dorsal attention network associated with broad band EEG power (Labounek et al., 2015; Laufs et al., 2003a; Laufs et al., 2003b), the default mode network (Labounek et al., 2015; Laufs et al., 2003a; Scheeringa et al., 2008), the speech network (Mareček et al., 2016), the sensory-motor network (Labounek et al., 2015, 2016) and the visual network (Labounek et al., 2015; Rosa et al., 2010).

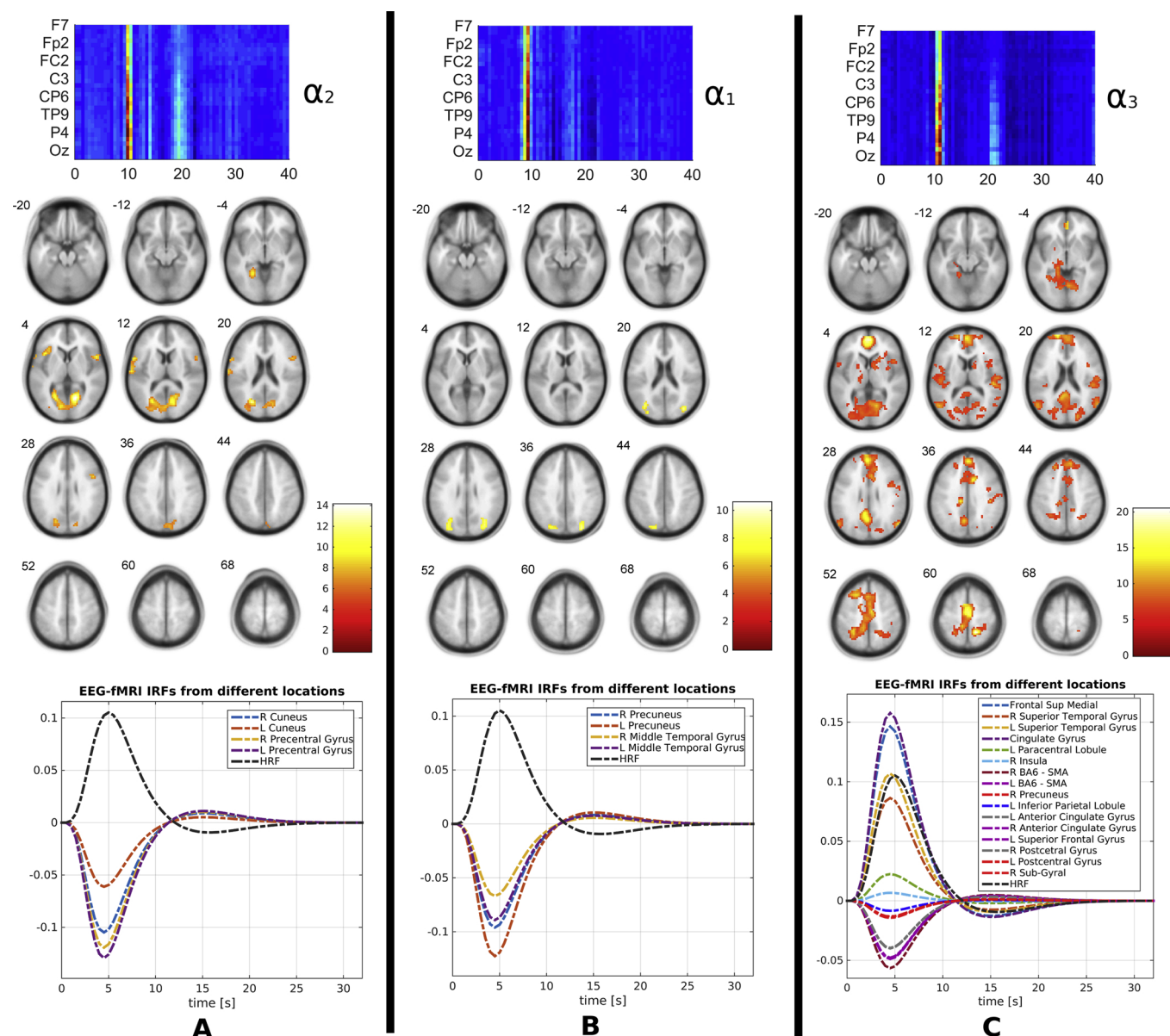


**Fig. 5.** Three different EEG-fMRI networks from the VOT task generated from three independent EEG spatiotemporal  $\alpha_{1-3}$ -band patterns and their local HRFs estimated with Eq. (9) from local maximums of the supra-threshold clusters. (A) Deactivations in primary visual cortices and bilateral precentral gyri correspond to EEG power increases for the map indicated in  $\alpha_2$ . HRFs were derived from the following MNI coordinates from the cluster: R Cuneus [15–67 4]mm, L Cuneus [-27–70 16]mm, R Precuneus [54 11 4]mm and L Precuneus [-60 8 10]mm. (B) Deactivations in the secondary visual cortices correspond to EEG power increases of the map indicated in  $\alpha_1$ . HRFs were derived from following MNI coordinates for the corresponding cluster: R Precuneus [30–76 34]mm, L Precuneus [-27–79 40]mm, R Middle Temporal Gyrus [36–76 22]mm and L Middle Temporal Gyrus [-36–76 22]mm. (C) Activations in the default mode network (DMN), left paracentral lobule and right insula and deactivations in sensory-motor areas, secondary visual cortices and left superior frontal gyrus were associated with fluctuations within the spatiotemporal map comprising  $\alpha_3$ . HRFs were derived from following MNI coordinates for the corresponding cluster: Frontal Sup Medial [0 53 4]mm, R Superior Temporal Gyrus [57–64 25]mm, L Superior Temporal Gyrus [-54–67 25]mm, Cingulate Gyrus [-3–58 28]mm, L Paracentral Lobule [-9–40 58]mm, R Insula [51–28 16]mm, R SMA [3–4 61]mm, L SMA [-3–7 58]mm, R Precuneus [15–49 61]mm, L Inferior Parietal Lobule [-27–46 55]mm; L Anterior Cingulate Gyrus [-12–25 37], R Anterior Cingulate Gyrus [12 14 34]mm, L Superior Frontal Gyrus [-30 20 55]mm, R Postcentral Gyrus [57–16 16]mm and L Postcentral Gyrus [-51–19 10]mm.

In the current study, the voxel-wise GLM between EEG spatiotemporal patterns and BOLD signals revealed supra-threshold F-maps that overlap spatially with several LSBNs (e.g. sensory-motor, basal ganglia, visual, default mode, salience and attention networks; Figs. 3–6 and Suppl. material). Although some similarities were observed over paradigms for some patterns, the most robust relationships between EEG and fMRI were observed during VOT. This finding may result due to the greater sample size within this dataset (21 subjects \* 4 sessions \* 256 scans) compared to the RST data (50 subjects \* 300 scans) or SDT data (42 subjects \* 230 scans), or the robustness of VOT responses that have been observed within the fMRI and EEG literature.

With respect to subcortical-networks, it is interesting to note that supra-threshold F-statistics overlap with the basal ganglia and the sensory motor network regions (Figs. 3, 4a, 5c and Suppl. material) primarily for low frequency EEG patterns (i.e. between the  $\delta$ -band up to the  $\alpha$ -band). For example, within the  $\delta$ -band, the maximum EEG-fMRI correlates are present within deep brain structures (Suppl. material) near the allocortex, where  $\delta$ -band generators (and  $\theta$ -band and  $\alpha$ -band generators) are thought to exist (Knyazev, 2012). Supra-threshold voxels are not present within the basal ganglia for the low  $\beta$ -band frequencies, where we instead observe a strong correspondence with voxels within left sensory-motor areas likely associated with the VOT

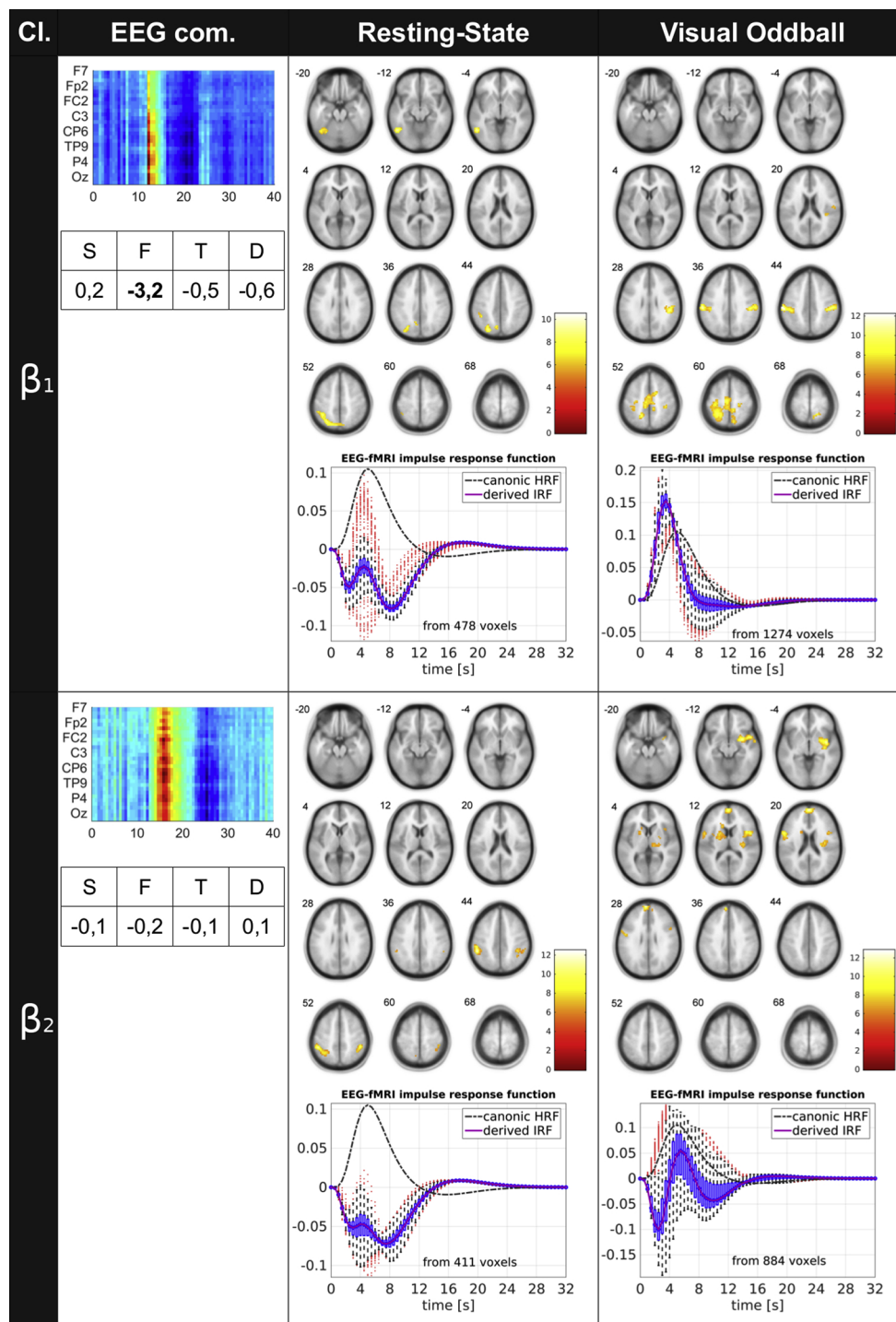


**Fig. 6.** EEG-fMRI group-averaged F-maps for EEG low and high  $\beta$ -band patterns for RST and VOT tasks, and HRFs derived from supra-threshold voxels. There were not any supra-threshold clusters for SDT data so only the RST and VOT results are shown. For the derived EEG-fMRI HRFs, the colorbar defines the F values in the corresponding F-map. In the plot below, the black dashed-dot line represents the canonical HRF, the purple line represents the median-derived HRF derived from the boxplots where blue oblongs are quartiles and the red dots are outliers. The values in the table under the spatiotemporal pattern are group-averaged t-values of statistical significance between the pattern's dynamics and stimulus vectors (S – sentence block in SDT, F – frequent, T – target, D – distractor in VOT).

right hand button press (Fig. 6, Table 2).

The observed antagonistic relationship between non- $\alpha$ -band and  $\alpha$ -band patterns and corresponding BOLD responses (Figs. 4a and 5c) is supported by (Pang and Robinson, 2018). EEG  $\alpha$ -band responses often demonstrate negative relationships with fMRI, since increase in the  $\alpha$ -band reflect neural disengagement (e.g. inhibition-timings hypothesis (Klimesch et al., 2007)) and a reduced metabolic state. This pattern is present for two of the stable  $\alpha_{1-2}$ -band spatiotemporal patterns which were associated with deactivations in primary (and secondary) visual cortices (Fig. 5a,b). Interestingly, we observed both positive and negative associations between the  $\alpha_3$ -band pattern and many fMRI regions, including activations within the default mode network, right

insula and left primary motor cortex of right foot, and the deactivations in the sensory-motor network, secondary visual and cognitive cortices (Fig. 5c). Since the EEG pattern was task-modulated (Table 2 and Suppl. material) the associated fMRI regions may contribute as follows: When a stimulus appears the activity in left lateralized sensory-motor cortices modulates (i.e. increases) activity in the right hand primary motor cortices. (Similar but less robust relationships were observed in secondary visual and cognition cortices.) At the same time, activity decreases in the default mode network, the right foot primary motor cortex (i.e. left paracentral lobule) and the right insula. Thus, these different regions are distinguished by their opposing relationships with concurrent EEG—increases in  $\alpha_3$ -band activity correspond to increases

**Table 2**

T-values of statistical significance between EEG spatirospectral pattern time courses and stimuli vectors from GLM. Cl. - cluster; S – semantic right or wrong sentence stimulus (probe block); F – frequent stimulus; T – target stimulus; D – distractor stimulus.

Cl.	S	F	T	D	Band
$\delta_1$	0.9	-1.2	0.4	-0.5	8
$\delta_2$	-0.6	-0.8	1.8	0.3	
$\delta_3$	-0.1	-1.5	<b>2.4</b>	0.2	
$\delta_4$	<b>-2.1</b>	<b>-2.1</b>	0.2	<b>-2.2</b>	
$\theta_1$	-1.6	-0.3	2.4	-0.2	θ
$\theta_2$	-0.2	-1.8	0.7	0.2	
$\theta_3$	-0.7	-1.1	-0.4	0.6	
$\theta_4$	-0.7	<b>-2.5</b>	-1.2	-0.8	
$\theta_5$	-1.5	0.4	0.4	-1.0	
$\alpha_1$	-0.9	1.7	<b>2.6</b>	0.6	α
$\alpha_2$	-1.1	1.6	0.7	0.1	
$\alpha_3$	-1.9	<b>2.5</b>	0.6	-0.3	
$\beta_1$	0.2	<b>-3.2</b>	-0.5	-0.6	β
$\beta_2$	-0.1	-1.1	0.1	0.5	
		-0.2	-0.1	0.1	

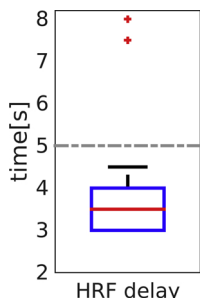


**Fig. 7.** Distribution of derived HRF absolute peak delays in comparison with the canonical HRF peak latency (the grey dashed line).

within one set of regions and decreases within another. Thus, we have demonstrated EEG-fMRI associations which are “*disjunctive*”, potentially as a result of opposing fMRI activations that relate to the task.

The timings over all three  $\alpha_{1-3}$ -band patterns (Fig. 5) more closely resemble the canonical HRF, consistent with the fact that the canonical HRF was derived from empirical measurements in visual cortex (Malonek and Grinvald, 1996), and consistent with  $\alpha$ -band HRF shapes demonstrated in previous studies (Bridwell et al., 2013; de Munck et al., 2007).

For the default mode network (Fig. 5c), the known associations between the fMRI BOLD signal and EEG spectral patterns appear heterogeneous and inconsistent within the literature. While we observed associations for the absolute power of the  $\alpha_3$ -band pattern, in concordance with (Bowman et al., 2015; Knyazev et al., 2011), we did not observe statistically significant associations that have been identified in previous studies, including the absolute frontal θ-band pattern (Scheeringa et al., 2008), the absolute δ-band pattern (Hlinka et al., 2010), the absolute β-band pattern (Hlinka et al., 2010; Laufs et al., 2003b), the relative α-band pattern (Hlinka et al., 2010; Labounek et al., 2015), the relative δ-band pattern and the relative β-band pattern (Hlinka et al., 2010).

The finding of associations between the attention network during RST and concurrent EEG spatirospectra (Figs. 4b, 6 and Suppl. material), is consistent with our previous concurrent findings (Mareček et al., 2017). However, we failed to observe EEG-fMRI relationships in dorsal attention networks using absolute power fluctuations (Labounek et al., 2015; Laufs et al., 2003b; Laufs et al., 2003a; Mareček et al., 2017).

#### 4.3. Current study novelty, limits and possible future work

To the best of our knowledge, this is the first study examining EEG-fMRI correlates after group-derived EEG spatirospectral decomposition over different experimental datasets. The voxel-wise EEG-fMRI approach revealed F-statistic fMRI overlays whose supra-threshold voxels organized into functional LSBNs consistent with previous literature. In addition, we have modeled spatially variable group-averaged HRFs often with shorter latency peaks than the canonical HRF (Figs. 3–7 and Suppl. material). It has been shown that spatially variable HRFs can reveal “opposite connectivity patterns” (Fig. 5c) characterized by fMRI voxels that relate to concurrent EEG spectra in opposing ways, with a subset of regions showing positive relationships and a subset of regions showing negative relationships. To investigate these relationships further, we may examine whether dynamics of spatirospectral patterns are related to dynamic functional connectivity among LSBNs, as demonstrated using PARAFAC EEG decomposition (Lamoš et al., 2018).

Although eye-blinking artifacts were previously observed only for  $\delta_4$ -band of the SDT dataset (Labounek et al., 2018), it seems that the artifact may be minimal, but present, within 11 of the 14 SDT components within the present study based on the peak responses over frontal regions (Fig. 2). This suggests that eye-blinking artifacts may not separate into a single component within spatirospectral group-ICA implemented in GIFT. This may result due to the variability of eye blink artifacts across subjects, motivating individual subject eye-blink artifact removal (e.g. with temporal ICA) prior to spatirospectral Group ICA. Alternatively, the Bayesian PARAFAC model appeared more successful at disentangling eye blinking artifacts within the SDT dataset here, potentially due to the different EEG preprocessing steps, including normalizing the signal amplitude separately for each frequency (Mareček et al., 2016). Overall, the issue of eye movements is an important consideration with respect to the SDT results in the present study, since individuals viewed sentences on the computer screen. In light of this potential artifact (which may have contributed to some of the stable components observed), it is important to consider whether the fMRI responses associated with SDT components may be related to eye movements and corresponding changes in visual activity.

The different sample sizes within the different tasks potentially limit the present study. Lower sample sizes within the RST and SDT tasks could have contributed to greater variability in the statistical estimates, potentially explaining the more robust EEG-fMRI associations observed within the VOT paradigm. In addition, we have included three different EEG-fMRI studies with different fMRI acquisition protocols and small differences in EEG recording. Since we have observed reasonable overlap among F-maps and EEG topographies across acquisitions, these findings appear robust to different fMRI protocols, despite this limitation.

Finally, previous research suggests that relative EEG power fluctuations contain greater task-related variability than absolute power fluctuations (Kilner et al., 2005; Klimesch, 1999; Labounek et al., 2015; Rosa et al., 2010; Scocco et al., 2014). The spatirospectral heuristic model (Labounek et al., 2016) could be implemented to preserve these task-related networks. However, there is a tradeoff between preserving EEG task-related variability and the stability of the EEG spatirospectral components, which decreases for relative power compared to absolute power (Labounek et al., 2018). Still even for the relative power, the spatirospectral group-ICA estimates are stable over paradigms, appear physiologically plausible, and demonstrate a closer relationship to the experimental time courses (Labounek et al., 2019).

#### 5. Conclusion

The present findings demonstrate that EEG-fMRI associations self-organize into structures of large scale brain networks. Using a flexible estimate of HRF shape, we show earlier HRF peak latency than the canonical HRF. The EEG-fMRI associations were more robust for the

visual oddball task, followed by the resting-state data and the semantic decision task. The reduced presence of EEG-fMRI associations for the SDT data were possibly due to the greater presence of eye-blinking artifacts within that dataset. Weak relationships between spatiotemporal time courses and task time courses (i.e. approaching uncorrected statistical significance ( $p < 0.05$ ) may result since the absolute EEG power was used as input into spatiotemporal group-ICA, as opposed to relative EEG power (Labounek et al., 2019).

## Acknowledgments

We would like to thank Dr. Milena Košťálová for her help with designing the semantic decision task. This research was supported by grants n. FEKT-S-14-2210 and FEKT-S-11-2-921 of Brno University of Technology, by grant n. CZ.1.05/1.1.00/02.0068 of Central European Institute of Technology and by grants n. NV16-30210A and NV17-29452A of Czech Health Research Council. The funding is highly acknowledged. Computational resources were provided by the MetaCentrum under the program LM2010005 and the CERIT-SC under the program Centre CERIT Scientific Cloud, part of the Operational Program Research and Development for Innovations, Reg. no. CZ.1.05/3.2.00/08.0144.

## Appendix A. Supplementary data

Supplementary material related to this article can be found, in the online version, at doi:<https://doi.org/10.1016/j.jneumeth.2019.02.012>.

## References

- Allen, P.J., Polizzi, G., Krakow, K., Fish, D.R., Lemieux, L., 1998. Identification of EEG events in the MR scanner: the problem of pulse artifact and a method for its subtraction. *Neuroimage* 8, 229–239. <https://doi.org/10.1006/nimg.1998.0361>.
- Allen, P.J., Josephs, O., Turner, R., 2000. A method for removing imaging artifact from continuous EEG recorded during functional MRI. *Neuroimage* 12, 230–239. <https://doi.org/10.1006/nimg.2000.0599>.
- Allen, E.A., Erhardt, E.B., Damaraju, E., Gruner, W., Segall, J.M., Silva, R.F., Havlicek, M., Rachakonda, S., Fries, J., Kalyanam, R., Michael, A.M., Caprihan, A., Turner, J., Eichele, T., Adelsheim, S., Bryan, A.D., Bustillo, J., Clark, V.P., Feldstein Ewing, S.W., Filbey, F., Ford, C.C., Hutchison, K., Jung, R.E., Kiehl, K.A., Kodituwakk, P., Komatsu, Y.M., Mayer, A.R., Pearson, G.D., Phillips, J.P., Sadek, J.R., Stevens, M., Teuscher, U., Thoma, R.J., Calhoun, V.D., 2011. A baseline for the multivariate comparison of resting-state networks. *Front. Syst. Neurosci.* 5, 2. <https://doi.org/10.3389/fnsys.2011.00002>.
- Anemüller, J., Sejnowski, T.J., Makeig, S., 2003. Complex independent component analysis of frequency-domain electroencephalographic data. *Neural Netw.* 16, 1311–1323. <https://doi.org/10.1016/j.neunet.2003.08.003>.
- Bell, A.J., Sejnowski, T.J., 1995. An information-maximization approach to blind separation and blind deconvolution. *Neural Comput.* 7, 1129–1159. <https://doi.org/10.1162/neco.1995.7.6.1129>.
- Bénar, C.-G., Schön, D., Grimault, S., Nazarian, B., Burle, B., Roth, M., Badier, J.-M., Marquis, P., Liegeois-Chauvel, C., Anton, J.-L., 2007. Single-trial analysis of oddball-related potentials in simultaneous EEG-fMRI. *Hum. Brain Mapp.* 28, 602–613. <https://doi.org/10.1002/hbm.20289>.
- Bowman, A., Griffis, J., Visscher, K., Dobbins, A., Gawne, T., DiFrancesco, M., Szaflarski, J., 2015. Alpha rhythm and the default mode network: an EEG/fMRI study. *Neurology* 84 P6. 021.
- Brázdil, M., Mikl, M., Mareček, R., Krupa, P., Rektor, I., Marecek, R., Krupa, P., Rektor, I., 2007. Effective connectivity in target stimulus processing: a dynamic causal modeling study of visual oddball task. *Neuroimage* 35, 827–835. <https://doi.org/10.1016/j.neuroimage.2006.12.020>.
- Bridwell, D.A., Wu, L., Eichele, T., Calhoun, V.D., 2013. The spatiotemporal characterization of brain networks: fusing concurrent EEG spectra and fMRI maps. *Neuroimage* 69, 101–111. <https://doi.org/10.1016/j.neuroimage.2012.12.024>.
- Bridwell, D.A., Rachakonda, S., Silva, R.F., Pearson, G.D., Calhoun, V.D., 2018. Spatiotemporal decomposition of multi-subject EEG: evaluating blind source separation algorithms on real and realistic simulated data. *Brain Topogr.* 31, 47–61. <https://doi.org/10.1007/s10548-016-0479-1>.
- Calhoun, V.D., Adali, T., Pearson, G.D., Pekar, J.J., 2001. A method for making group inferences from functional MRI data using independent component analysis. *Hum. Brain Mapp.* 14, 140–151. <https://doi.org/10.1002/hbm>.
- Calhoun, V.D., Kiehl, K.A., Pearson, G.D., 2008. Modulation of temporally coherent brain networks estimated using ICA at rest and during cognitive tasks. *Hum. Brain Mapp.* 29, 828–838. <https://doi.org/10.1002/hbm.20581>.
- Cavanagh, J.F., Frank, M.J., 2014. Frontal theta as a mechanism for cognitive control. *Trends Cogn. Sci.* 18, 414–421. <https://doi.org/10.1016/j.tics.2014.04.012>.
- Cong, F., He, Z., Hämäläinen, J., Leppänen, P.H.T., Lyytinen, H., Cichocki, A., Ristaniemi, T., 2013. Validating rationale of group-level component analysis based on estimating number of sources in EEG through model order selection. *J. Neurosci. Methods* 212, 165–172. <https://doi.org/10.1016/j.jneumeth.2012.09.029>.
- Congedo, M., John, R.E., De Ridder, D., Prichard, L., 2010. Group independent component analysis of resting state EEG in large normative samples. *Int. J. Psychophysiol.* 78, 89–99. <https://doi.org/10.1016/j.ijpsycho.2010.06.003>.
- Damoiseaux, J.S., Rombouts, S.A.R.B., Barkhof, F., Scheltens, P., Stam, C.J., Smith, S.M., Beckmann, C.F., 2006. Consistent resting-state networks across healthy subjects. *Proc. Natl. Acad. Sci. U. S. A.* 103, 13848–13853. <https://doi.org/10.1073/pnas.0601417103>.
- de Munck, J.C.C., Gonçalves, S.I.I., Huijboom, L., Kuijzer, J.P.A.P.A., Pouwels, P.J.W.J.W., Heethaar, R.M.M., Lopes da Silva, F.H.H., 2007. The hemodynamic response of the alpha rhythm: an EEG/fMRI study. *Neuroimage* 35, 1142–1151. <https://doi.org/10.1016/j.neuroimage.2007.01.022>.
- de Munck, J.C., Gonçalves, S.I., Mamoliti, R., Heethaar, R.M., Lopes da Silva, F.H., 2009. Interactions between different EEG frequency bands and their effect on alpha-fMRI correlations. *Neuroimage* 47, 69–76. <https://doi.org/10.1016/j.neuroimage.2009.04.029>.
- Eichele, T., Rachakonda, S., Brakedal, B., Eikeland, R., Calhoun, V.D., 2011. EEGIFT: group independent component analysis for event-related EEG data. *Comput. Intell. Neurosci.* <https://doi.org/10.1155/2011/129365>.
- Friston, K.J., Holmes, A.P., Worsley, K.J., Poline, J.-P., Frith, C.D., Frackowiak, R.S.J., 1994. Statistical parametric maps in functional imaging: a general linear approach. *Hum. Brain Mapp.* 2, 189–210. <https://doi.org/10.1002/hbm.460020402>.
- Friston, K.J., Ashburner, J., Frith, C.D., Poline, J., Heather, J.D., Frackowiak, R.S.J., 1995. Spatial registration and normalization of images. *Hum. Brain Mapp.* 3, 165–189.
- Friston, K.J., Fletcher, P., Josephs, O., Holmes, A., Rugg, M.D., Turner, R., 1998. Event-related fMRI: characterizing differential responses. *Neuroimage* 7, 30–40. <https://doi.org/10.1006/nimg.1997.0306>.
- Gartus, A., Foki, T., Geissler, A., Beisteiner, R., 2009. Improvement of clinical language localization with an overt semantic and syntactic language functional MR imaging paradigm. *Am. J. Neuroradiol.* 30, 1977–1985. <https://doi.org/10.3174/jnr.A1725>.
- Gevins, A.S., Zeitlin, G.M., Yingling, C.D., Doyle, J.C., Dedon, M.F., Schaffer, R.E., Roumasset, J.T., Yeager, C.L., 1979. EEG Patterns during “cognitive” tasks. I. Methodology and analysis of complex behaviours. *Electroencephalogr. Clin. Neurophysiol.* 47, 693–703.
- Goldman, R.I., Stern, J.M., Engel, J.J., Cohen, M.S., 2002. Simultaneous EEG and fMRI of alpha rhythm. *Neuroreport* 13, 2487–2492. <https://doi.org/10.1097/01.wnr.0000047685.08940.d0>.
- Hiltunen, T., Kantola, J., Abou Elseoud, A., Lepola, P., Suominen, K., Starck, T., Nikkinen, J., Remes, J., Tervonen, O., Palva, S., Kiviniemi, V., Palva, J.M., 2014. Infra-slow EEG fluctuations are correlated with resting-state network dynamics in fMRI. *J. Neurosci.* 34, 356–362. <https://doi.org/10.1523/JNEUROSCI.0276-13.2014>.
- Himberg, J., Hyvärinen, A., Esposito, F., 2004. Validating the independent components of neuroimaging time series via clustering and visualization. *Neuroimage* 22, 1214–1222. <https://doi.org/10.1016/j.neuroimage.2004.03.027>.
- Hlinka, J., Alexakis, C., Diukova, A., Liddle, P.F., Auer, D.P., 2010. Slow EEG pattern predicts reduced intrinsic functional connectivity in the default mode network: an inter-subject analysis. *Neuroimage* 53, 239–246. <https://doi.org/10.1016/j.neuroimage.2010.06.002>.
- Huster, R.J., Calhoun, V.D., 2018. Progress in EEG: multi-subject decomposition and other advanced signal processing approaches. *Brain Topogr.* 31, 1–2. <https://doi.org/10.1007/s10548-017-0616-5>.
- Huster, R.J., Raud, L., 2018. A tutorial review on multi-subject decomposition of EEG. *Brain Topogr.* 31 (1), 3–16.
- Huster, R.J., Plis, S.M., Calhoun, V.D., 2015. Group-level component analyses of EEG: validation and evaluation. *Front. Neurosci.* 9, 254. <https://doi.org/10.3389/fnins.2015.00254>.
- Hyvärinen, A., Ramkumar, P., Parkkonen, L., Hari, R., 2010. Independent component analysis of short-time Fourier transforms for spontaneous EEG/MEG analysis. *Neuroimage* 49, 257–271. <https://doi.org/10.1016/j.neuroimage.2009.08.028>.
- Jacobs, J., LeVan, P., Moeller, F., Boor, R., Stephani, U., Gotman, J., Siniatchkin, M., 2009. Hemodynamic changes preceding the interictal EEG spike in patients with focal epilepsy investigated using simultaneous EEG-fMRI. *Neuroimage* 45, 1220–1231. <https://doi.org/10.1016/j.neuroimage.2009.01.014>.
- Jensen, O., Tesche, C.D., 2002. Frontal theta activity in humans increases with memory load in a working memory task. *Eur. J. Neurosci.* 15, 1395–1399. <https://doi.org/10.1046/j.1460-9568.2002.01975.x>.
- Keinänen, T., Rytty, S., Korhonen, V., Huotari, N., Nikkinen, J., Tervonen, O., Palva, J.M., Kiviniemi, V., 2018. Fluctuations of the EEG-fMRI correlation reflect intrinsic strength of functional connectivity in default mode network. *J. Neurosci. Res.* 96, 1689–1698. <https://doi.org/10.1002/jnr.24257>.
- Kilner, J.M.M., Mattout, J., Henson, R., Friston, K.J.J., 2005. Hemodynamic correlates of EEG: a heuristic. *Neuroimage* 28, 280–286. <https://doi.org/10.1016/j.neuroimage.2005.06.008>.
- Klimesch, W., 1999. EEG alpha and theta oscillations reflect cognitive and memory performance: a review and analysis. *Brain Res. Rev.* 29, 169–195. [https://doi.org/10.1016/S0165-0173\(98\)00056-3](https://doi.org/10.1016/S0165-0173(98)00056-3).
- Klimesch, W., Sauseng, P., Hanslmayr, S., 2007. EEG alpha oscillations: the inhibition-timing hypothesis. *Brain Res. Rev.* 53, 63–88. <https://doi.org/10.1016/j.brainresrev.2006.06.003>.
- Knyazev, G.G., 2012. EEG delta oscillations as a correlate of basic homeostatic and motivational processes. *Neurosci. Biobehav. Rev.* 36, 677–695. <https://doi.org/10.1016/j.neubiorev.2011.10.002>.

- Knyazev, G.G., Slobodskoj-Plusnin, J.Y., Bocharov, A.V., Pylkova, L.V., 2011. The default mode network and EEG alpha oscillations: an independent component analysis. *Brain Res.* 1402, 67–79. <https://doi.org/10.1016/j.brainres.2011.05.052>.
- Kovacevic, N., McIntosh, A.R., 2007. Groupwise independent component decomposition of EEG data and partial least square analysis. *Neuroimage* 35, 1103–1112. <https://doi.org/10.1016/j.neuroimage.2007.01.016>.
- Labounek, R., Lamoš, M., Mareček, R., Brázdił, M., Jan, J., 2015. Exploring task-related variability in fMRI data using fluctuations in power spectrum of simultaneously acquired EEG. *J. Neurosci. Methods* 245, 125–136. <https://doi.org/10.1016/j.jneumeth.2015.02.016>.
- Labounek, R., Janeček, D., Mareček, R., Lamoš, M., Slavíček, T., Mikl, M., Baštinec, J., Bednářík, P., Bridwell, D., Brázdił, M., Jan, J., 2016. Generalized EEG-fMRI spectral and spatiotemporal heuristic models. 13th International Symposium on Biomedical Imaging: From Nano to Macro 767–770. <https://doi.org/10.1109/ISBI.2016.7493379>.
- Labounek, R., Bridwell, D.A., Mareček, R., Lamoš, M., Mikl, M., Slavíček, T., Bednářík, P., Baštinec, J., Hluštík, P., Brázdił, M., Jan, J., 2018. Stable scalp EEG spatiotemporal patterns across paradigms estimated by group ICA. *Brain Topogr.* 31, 76–89. <https://doi.org/10.1007/s10548-017-0585-8>.
- Labounek, R., Bridwell, D.A., Mareček, R., Lamoš, M., Mikl, M., Brázdił, M., Jan, J., Hluštík, P., 2019. Stable EEG spatiotemporal sources using relative power as group-ICA input. *IFMBE Proc. World Congr. Med. Phys. Biomed. Eng.* 68, 125–128. <https://doi.org/10.1007/978-981-10-9035-6>.
- Lamoš, M., Mareček, R., Slavíček, T., Mikl, M., Rektor, I., Jan, J., 2018. Spatial-temporal-spectral EEG patterns of BOLD functional network connectivity dynamics. *J. Neural Eng.* 15, 036025.
- Laufs, H., Kleinschmidt, A., Beyerle, a, Eger, E., Salek-Haddadi, A., Preibisch, C., Krakow, K., 2003a. EEG-correlated fMRI of human alpha activity. *Neuroimage* 19, 1463–1476. [https://doi.org/10.1016/S1053-8119\(03\)00286-6](https://doi.org/10.1016/S1053-8119(03)00286-6).
- Laufs, H., Krakow, K., Sterzer, P., Eger, E., Beyerle, A., Salek-Haddadi, A., Kleinschmidt, A., 2003b. Electroencephalographic signatures of attentional and cognitive default modes in spontaneous brain activity fluctuations at rest. *Proc. Natl. Acad. Sci.* 100, 11053–11058. <https://doi.org/10.1073/pnas.1831638100>.
- Lemieux, L., Salek-Haddadi, A., Josephs, O., Allen, P., Toms, N., Scott, C., Krakow, K., Turner, R., Fish, D.R., 2001. Event-related fMRI with simultaneous and continuous EEG: description of the method and initial case report. *Neuroimage* 14, 780–787. <https://doi.org/10.1006/nimg.2001.0853>.
- Lio, G., Boulinguez, P., 2013. Greater robustness of second order statistics than higher order statistics algorithms to distortions of the mixing matrix in blind source separation of human EEG: implications for single-subject and group analyses. *Neuroimage* 67, 137–152. <https://doi.org/10.1016/j.neuroimage.2012.11.015>.
- Malonek, D., Grinvald, A., 1996. Interactions between electrical activity and cortical microcirculation revealed by imaging spectroscopy: implications for functional brain mapping. *Science* 80, 272–251.
- Mantini, D., Perrucci, M.G., Del Gratta, C., Romani, G.L., Corbetta, M., 2007. Electrophysiological signatures of resting state networks in the human brain. *Proc. Natl. Acad. Sci. U. S. A.* 104, 13170–13175. <https://doi.org/10.1073/pnas.0700668104>.
- Mantini, D., Corbetta, M., Perrucci, M.G., Romani, G.L., Del Gratta, C., 2009. Large-scale brain networks account for sustained and transient activity during target detection. *Neuroimage* 44, 265–274. <https://doi.org/10.1016/j.neuroimage.2008.08.019>.
- Mantini, D., Marzetti, L., Corbetta, M., Romani, G.L., Del Gratta, C., 2010. Multimodal integration of fMRI and EEG data for high spatial and temporal resolution analysis of brain networks. *Brain Topogr.* 23, 150–158. <https://doi.org/10.1007/s10548-009-0132-3>.
- Mareček, R., Lamoš, M., Mikl, M., Bartoň, M., Fajkus, J., Rektor, I., Brázdił, M., 2016. What can be found in scalp EEG spectrum beyond common frequency bands. EEG-fMRI study. *J. Neural Eng.* 13, 1–13. <https://doi.org/10.1088/1741-2560/13/4/046026>.
- Mareček, R., Lamoš, M., Labounek, R., Bartoň, M., Slavíček, T., Mikl, M., Rektor, I., Brázdił, M., 2017. Multiway array decomposition of EEG spectrum: implications of its stability for the exploration of large-scale brain networks. *Neural Comput.* 29, 968–989. [https://doi.org/10.1162/NECO\\_a\\_00933](https://doi.org/10.1162/NECO_a_00933).
- Moosmann, M., Eichele, T., Nordby, H., Hugdahl, K., Calhoun, V.D., 2008. Joint independent component analysis for simultaneous EEG-fMRI: principle and simulation. *Int. J. Psychophysiol.* 67, 212–221. <https://doi.org/10.1016/j.ijpsycho.2007.05.016>.
- Mulert, C., Jäger, L., Schmitt, R., Bussfeld, P., Pogarell, O., Möller, H.-J., Juckel, G., Hegerl, U., 2004. Integration of fMRI and simultaneous EEG: towards a comprehensive understanding of localization and time-course of brain activity in target detection. *Neuroimage* 22, 83–94. <https://doi.org/10.1016/j.neuroimage.2003.10.051>.
- Nikulin, V.V., Nolte, G., Curio, G., 2011. A novel method for reliable and fast extraction of neuronal EEG/MEG oscillations on the basis of spatio-spectral decomposition. *Neuroimage* 55, 1528–1535. <https://doi.org/10.1016/j.neuroimage.2011.01.057>.
- Onton, J., Delorme, A., Makeig, S., 2005. Frontal midline EEG dynamics during working memory. *Neuroimage* 27, 341–356. <https://doi.org/10.1016/j.neuroimage.2005.04.014>.
- Pang, J.C., Robinson, P.A., 2018. Neural mechanisms of the EEG alpha-BOLD anticorrelation. *Neuroimage* 181, 461–470. <https://doi.org/10.1016/j.neuroimage.2018.07.031>.
- Portnova, G., Balaev, V., Tetereva, A., Atanov, M., Ivanitsky, A., Skiteva, L., Ushakov, V., Martynova, O., 2018. Correlation of BOLD signal with linear and nonlinear patterns of EEG in resting state EEG-informed fMRI. *Front. Hum. Neurosci.* 11, 654. <https://doi.org/10.3389/fnhum.2017.00654>.
- Ramkumar, P., Parkkonen, L., Hari, R., Hyvärinen, A., 2012. Characterization of neuro-magnetic brain rhythms over time scales of minutes using spatial independent component analysis. *Hum. Brain Mapp.* 33, 1648–1662. <https://doi.org/10.1002/hbm.21303>.
- Ramkumar, P., Parkkonen, L., Hyvärinen, A., 2014. Group-level spatial independent component analysis of Fourier envelopes of resting-state MEG data. *Neuroimage* 86, 480–491. <https://doi.org/10.1016/j.neuroimage.2013.10.032>.
- Rosa, M.J., Kilner, J., Blankenburg, F., Josephs, O., Penny, W., 2010. Estimating the transfer function from neuronal activity to BOLD using simultaneous EEG-fMRI. *Neuroimage* 49, 1496–1509. <https://doi.org/10.1016/j.neuroimage.2009.09.011>.
- Salek-Haddadi, A., Diehl, B., Hamandi, K., Merschhemke, M., Liston, A., Friston, K., Duncan, J.S., Fish, D.R., Lemieux, L., 2006. Hemodynamic correlates of epileptiform discharges: an EEG-fMRI study of 63 patients with focal epilepsy. *Brain Res.* 1088, 148–166. <https://doi.org/10.1016/j.brainres.2006.02.098>.
- Sammer, G., Blecker, C., Gebhardt, H., Bischoff, M., Stark, R., Morgen, K., Vaitl, D., 2007. Relationship between regional hemodynamic activity and simultaneously recorded EEG-theta associated with mental arithmetic-induced workload. *Hum. Brain Mapp.* 28, 793–803. <https://doi.org/10.1002/hbm.20309>.
- Scheeringa, R., Bastiaansen, M.C.M., Petersson, K.M., Oostenveld, R., Norris, D.G., Hagoort, P., 2008. Frontal theta EEG activity correlates negatively with the default mode network in resting state. *Int. J. Psychophysiol.* 67, 242–251. <https://doi.org/10.1016/j.ijpsycho.2007.05.017>.
- Sclocco, R., Tana, M.G., Visani, E., Giloli, I., Panzica, F., Franceschetti, S., Cerutti, S., Bianchi, A.M., 2014. EEG-informed fMRI analysis during a hand grip task: estimating the relationship between EEG rhythms and the BOLD signal. *Front. Hum. Neurosci.* 8, 186. <https://doi.org/10.3389/fnhum.2014.00186>.
- Shou, G., Ding, L., Dasari, D., 2012. Probing neural activations from continuous EEG in a real-world task: time-frequency independent component analysis. *J. Neurosci. Methods* 209, 22–34. <https://doi.org/10.1016/j.jneumeth.2012.05.022>.
- Spadone, S., Della Penna, S., Sestieri, C., Betti, V., Tosoni, A., Perrucci, M.G., Romani, G.L., Corbetta, M., 2015. Dynamic reorganization of human resting-state networks during visuospatial attention. *Proc. Natl. Acad. Sci. U. S. A.* 112, 8112–8117. <https://doi.org/10.1073/pnas.1415439112>.
- Van Den Heuvel, M.P., Mandl, R.C.W., Kahn, R.S., Hulshoff Pol, H.E., 2009. Functionally linked resting-state networks reflect the underlying structural connectivity architecture of the human brain. *Hum. Brain Mapp.* 30, 3127–3141. <https://doi.org/10.1002/hbm.20737>.
- Vulliemoz, S., Rodionov, R., Carmichael, D.W., Thornton, R., Guye, M., Lhatoo, S.D., Michel, C.M., Duncan, J.S., Lemieux, L., 2010. Continuous EEG source imaging enhances analysis of EEG-fMRI in focal epilepsy. *Neuroimage* 49, 3219–3229. <https://doi.org/10.1016/j.neuroimage.2009.11.055>.
- Wu, L., Eichele, T., Calhoun, V.D., 2010. Reactivity of hemodynamic responses and functional connectivity to different states of alpha synchrony: a concurrent EEG-fMRI study. *Neuroimage* 52, 1252–1260. <https://doi.org/10.1016/j.neuroimage.2010.05.053>.